J Geod
DOI 10.1007/s00190-013-0688-2

ORIGINAL ARTICLE

GNSS antenna array-aided CORS ambiguity resolution

Bofeng Li · Peter J. G. Teunissen

Received: 19 August 2013 / Accepted: 12 December 2013

Abstract Array-aided precise point positioning is a measurement concept that uses GNSS data, from multiple antennas in an array of known geometry, to realize improved GNSS parameter estimation proposed by Teunissen (IEEE Trans Signal Process 60:2870–2881, 2012). In this contribution, the benefits of array-aided CORS ambiguity resolution are explored. The mathematical model is formulated to show how the platform-array data can be reduced and how the variance matrix of the between-platform ambiguities can profit from the increased precision of the reduced platform data. The ambiguity resolution performance will be demonstrated for varying scenarios using simulation. We consider single-, dual- and triple-frequency scenarios of geometry-based and geometry-free models for different number of antennas and different standard deviations of the ionosphere-weighted constraints. The performances of both full and partial ambiguity resolution (PAR) are presented for these different scenarios. As the study shows, when full advantage is taken of the array antennas, both full and partial ambiguity resolution can be significantly improved, in some important cases even enabling instantaneous ambiguity resolution. PAR widelaning and its suboptimal character are hereby also illustrated.

B. Li (✉) · P. J. G. Teunissen
College of Surveying and Geo-Informatics, Tongji University, Shanghai, People's Republic of China
e-mail: bofeng_li@tongji.edu.cn; bofeng_li@163.com

B. Li · P. J. G. Teunissen
GNSS Research Centre, Curtin University, Perth, Australia

P. J. G. Teunissen
Geoscience and Remote Sensing, Delft University of Technology, Delft, Netherlands
e-mail: p.teunissen@curtin.edu.au

Keywords Global navigation satellite system (GNSS) · Integer ambiguity resolution (IAR) · Continuously operating reference station (CORS) · Array-aided precise point positioning (A-PPP) · Full ambiguity resolution (FAR) · Partial ambiguity resolution (PAR)

1 Introduction

Integer ambiguity resolution is the key to high-precision GNSS applications. It enables the transformation of the ambiguous carrier phases to ultra-precise pseudoranges, thus making high-precision parameter estimation possible. The success of ambiguity resolution depends on the strength of the underlying GNSS model. The weaker the model, the more data needs to be accumulated before ambiguity resolution can be successful and the longer it therefore takes before one can take advantage of the ultra-precise carrier signals. Clearly, the aim is to shorten the time to convergence, preferably zero, thereby enabling truly instantaneous GNSS, integer ambiguity resolved, parameter estimation.

In CORS network applications, fast and successful resolution of the ambiguities is important as it enables improved availability of the network provided ambiguity-fixed parameter outputs, such as the ionospheric delays. Between-station ambiguity resolution is usually based on data of stations equipped with a single antenna only. In this contribution, we study the potential improvements that can be realized when stations would be equipped with an array of antennas instead of only a single antenna. This A-PPP concept, proposed in Teunissen (2012), is a measurement concept that uses GNSS data, from multiple antennas in an array of known geometry, to realize improved GNSS parameter estimation. Although we focus on ambiguity resolution in this contribution, integrity improves, since with the known array geom-

Published online: 31 December 2013

Fig. 1 Two antenna-array equipped platforms b_0 and u_0

etry, redundancy increases, thus allowing improved error detection and multipath mitigation (Teunissen 1998a; Ray et al 2000).

Consider Fig. 1, in which two antenna-array equipped stations, b_0 and u_0, are shown. The two antenna arrays, with known geometry, $b_1, \ldots, b_r$ and $u_1, \ldots, u_r$, are mounted on the platforms at b_0 and u_0, respectively. The known platform antenna-array geometry enables one to reduce the platform observations of all its antennas to a single set of platform observations. This set of reduced observations can be interpreted as if it belongs to one single virtual antenna with a better precision than the original observations coming from the individual antennas. Therefore, improved between-platform $(b_0 - u_0)$ ambiguity resolution and parameter estimation become possible as compared to the between-platform single-antenna case. This improvement has been initially demonstrated on long-distance RTK campaign (Li and Teunissen 2012). Although the reduction of the platform observations also requires ambiguity resolution, namely on the platform, this can be shown possible with high success rates due to the known antenna-array geometry (Giorgi et al 2010).

In Teunissen (2012), one of the potential applications of A-PPP is to speed up the CORS ambiguity resolution. In this contribution, we comprehensively explore the potential benefits of A-PPP to the CORS network ambiguity resolution. As CORS stations are usually well-selected sites, with receiver equipment costs being a fraction of the overall CORS-station costs, the required multi-antenna extension of CORS is expected feasible. This contribution is organized as follows. In Sect. 2, we formulate the platform array model and show how its data can be reduced. In Sect. 3, we describe three different ionosphere-weighted differential CORS array models and present closed form formulae for their ambiguity variance matrices. They determine the success rates with which the integer ambiguities can be estimated. The A-PPP CORS simulation results are presented and analyzed in Sect. 4. This is done for different scenarios, such as for single-, dual- and triple-frequency, geometry-based and geometry-free models, with varying ionosphere-weighted constraints. Finally, the conclusions are given in Sect. 5.

In following, I_n denotes the identity matrix of order n and e_n the n-column vector with 1s. $c_1 = [1, 0, \ldots, 0]^T$ is a unit vector with its 1 in the first slot. $D_n^T = [-e_{n-1}, I_{n-1}]$ is the differencing matrix. $\otimes$ and vec are Kronecker product and vectorization operators. E and D denote the expectation and dispersion operators. $\mathsf{diag}(a)$ is the operator to form a square matrix with elements of a as diagonal elements.

2 Platform array model and its data reduction

2.1 The functional model

We start with the linearized single-frequency, between-satellite single-differenced (SD) observation equations of phase and code,

$$\begin{aligned} \mathsf{E}(\phi_{r,j}) &= G_r x_r + g_r \tau_r - \mu_j \iota_r - \delta t_{,j} + \lambda_j a_{r,j} \\ \mathsf{E}(p_{r,j}) &= G_r x_r + g_r \tau_r + \mu_j \iota_r - dt_{,j} \end{aligned} \tag{1}$$

where the subscripts r and j denote the antenna and the frequency f_j (wavelength λ_j), which are used to emphasize the antenna-specific and frequency-specific terms, respectively. Assuming that $(s+1)$ satellites are simultaneously tracked, $\phi_{r,j} = [\phi_{r,j}^1, \ldots, \phi_{r,j}^s]^T$ and $p_{r,j} = [p_{r,j}^1, \ldots, p_{r,j}^s]^T$ are the $(s \times 1)$ SD phase and code observation vectors; G_r is the $(s \times 3)$ design matrix of the unknown baseline increment vector x_r; τ_r is the zenith tropospheric delay (ZTD), with its mapping matrix g_r; $\iota_r = [\iota_r^1, \ldots, \iota_r^s]^T$ is the $(s \times 1)$ vector of SD ionospheric delays on frequency f_1 with $\mu_j = f_1^2/f_j^2$; $\delta t_{,j} = [\delta t_{,j}^1, \ldots, \delta t_{,j}^s]^T$ and $dt_{,j} = [dt_{,j}^1, \ldots, dt_{,j}^s]^T$ are the SD satellite clock errors for phase and code, respectively; $a_{r,j} = [a_{r,j}^1, \ldots, a_{r,j}^s]^T$ is the $(s \times 1)$ SD ambiguity vector with the sth element $a_{r,j}^s = z_{r,j}^s - \varphi_{,j}^s(t_0)$, where $z_{r,j}^s$ is integer and $\varphi_{,j}^s(t_0)$ is real-valued.

For f frequencies, we define the vectors, $y_r = [\phi_r^T,\ p_r^T]^T$ and $\Delta t = [\delta t^T,\ dt^T]^T$, with $\phi_r = [\phi_{r,1}^T, \ldots, \phi_{r,f}^T]^T$, $\delta t = [\delta t_{,1}^T, \ldots, \delta t_{,f}^T]^T$; where p_r and dt have the same structure as ϕ_r and δt, respectively. Furthermore, $\mu = [\mu_1, \ldots, \mu_f]^T$, $a_r = [a_{r,1}^T, \ldots, a_{r,f}^T]^T$ and $\Lambda = \mathsf{diag}(\lambda_1, \ldots, \lambda_f)$.

Since we assume the distances between the antennas on the platform to be very short, we may assume that $G_i = G$, $g = g_i$, $\tau = \tau_i$ and $\iota = \iota_i$ for $i = 1, \ldots, r$. This implies that we may write the r antenna array set of SD observation equations of (1) in multivariate form as

$$\mathsf{E}(Y) = MX + NA + e_r^T \otimes \left(\nu \otimes \iota + e_{2f} \otimes (g\tau) - \Delta t\right) \tag{2}$$

where $Y = [y_1, \ldots, y_r]$, $M = e_{2f} \otimes G$, $X = [x_1, \ldots, x_r]$, $N = \Gamma \otimes I_s$, $\Gamma = [\Lambda, 0]^T$, $A = [a_1, \ldots, a_r]$ and $\nu = [-\mu^T, \mu^T]^T$.

If we now post-multiply (2) with the invertible matrix $R_r = [c_1, D_r]$, we obtain with $[y_1, \tilde{Y}] = Y R_r$,

$$\mathsf{E}\begin{bmatrix} y_1 \\ \tilde{Y} \end{bmatrix} = \begin{bmatrix} Mx_1 + Na_1 + \nu \otimes \iota + (e_{2f} \otimes g)\tau - \Delta t \\ M\tilde{X} + NZ \end{bmatrix} \quad (3)$$

where $\tilde{Y} = [y_{12}, \ldots, y_{1r}]$ is the transformed double differenced (DD) observation matrix, $\tilde{X} = XD_r = [x_{12}, \ldots, x_{1r}]$ is the baseline matrix, and $Z = AD_r = [z_{12}, \ldots, z_{1r}]$ is the integer DD ambiguity matrix.

2.2 The stochastic model

We specify the stochastic model of $Y = [y_1, \ldots, y_r]$ as

$$\mathsf{D}(\mathrm{vec}(Y)) = Q_r \otimes Q \quad \text{with} \quad Q = Q_f \otimes (D_{s+1}^T Q_s D_{s+1}) \quad (4)$$

where Q_r captures the antenna-specific precision contribution, Q_s is the satellite elevation-dependent *cofactor* matrix of the $(s+1)$ *undifferenced* observations, and $Q_f = \mathsf{blockdiag}(Q_\phi, Q_p)$ captures the frequency-specific precision contribution, with $Q_\phi = \mathsf{diag}(\sigma^2_{\phi;1}, \ldots, \sigma^2_{\phi;f})$ and $Q_p = \mathsf{diag}(\sigma^2_{p;1}, \ldots, \sigma^2_{p;f})$, where $\sigma^2_{\phi;j}$ and $\sigma^2_{p;j}$ are the variance scalars of the undifferenced phase and code on frequency j, respectively.

Application of the variance propagation law to $[y_1, \tilde{Y}] = Y R_r$ gives, referring to Appendix A, the stochastic model of (3) as

$$\mathsf{D}\begin{bmatrix} y_1 \\ \mathrm{vec}(\tilde{Y}) \end{bmatrix} = \begin{bmatrix} c_1^T Q_r c_1 & c_1^T Q_r D_r \\ D_r^T Q_r c_1 & D_r^T Q_r D_r \end{bmatrix} \otimes Q \quad (5)$$

2.3 Array data reduction

From (5) it follows that y_1 and $\tilde{Y}$ of (3) are correlated. As shown by Teunissen (2012), application of the invertible transformation

$$\begin{bmatrix} 1 & -c_1^T Q_r D_r (D_r^T Q_r D_r)^{-1} \\ 0 & I_{r-1} \end{bmatrix} \otimes I_{2fs} \quad (6)$$

to (3), referring to Appendix A, results in the equivalent but decorrelated version

$$\mathsf{E}\begin{bmatrix} \bar{y} \\ \tilde{Y} \end{bmatrix} = \begin{bmatrix} M\bar{x} + N\bar{z} + (e_{2f} \otimes g)\tau + \nu \otimes \iota - \Delta t \\ M\tilde{X} + NZ \end{bmatrix} \quad (7)$$

where $[\bar{y}, \bar{x}] = [Y, X]Q_r^{-1} e_r (e_r^T Q_r^{-1} e_r)^{-1}$ and $\bar{z} = a_1 - ZD_r^+ c_1$, with $D_r^+ = (D_r^T Q_r D_r)^{-1} D_r^T Q_r$. The dispersion of the reduced observation vector $\bar{y}$ and the DD observation matrix $\tilde{Y}$ is given as

$$\mathsf{D}\begin{bmatrix} \bar{y} \\ \mathrm{vec}(\tilde{Y}) \end{bmatrix} = \begin{bmatrix} (e_r^T Q_r^{-1} e_r)^{-1} & 0 \\ 0 & D_r^T Q_r D_r \end{bmatrix} \otimes Q \quad (8)$$

showing that $\bar{y}$ is uncorrelated with $\tilde{Y}$.

In the following, we assume that the same type of antennas are used. Thus $Q_r = I_r$, from which it follows that $\bar{y} = \frac{1}{r}\sum_{i=1}^r y_i$, $\bar{x} = \frac{1}{r}\sum_{i=1}^r x_i$, $\bar{z} = a_1 + \frac{1}{r} Z e_{r-1}$, and $(e_r^T Q_r^{-1} e_r)^{-1} = 1/r$. The reduced observation vector $\bar{y}$ is thus r times more precise than that of a single antenna.

In case of an APPP-CORS platform, the barycentric position vector $\bar{x}$ is known, since the position vectors x_i of the platform antennas are assumed known. Furthermore, the known geometry $\tilde{X}$ of the antenna configuration on the platform enables one to determine the integer matrix estimator $\check{Z}$ of Z with a very high success rate, see Teunissen (2012). Hence, for all practical purposes one may also assume the DD integer matrix Z in $\bar{z} = a_1 + \frac{1}{r} Z e_{r-1}$ known. Therefore, with $\bar{x}$ and Z known, the first equation of (7) can now be written as

$$\mathsf{E}(y') = (e_{2f} \otimes g)\tau + \nu \otimes \iota + Na_1 - \Delta t \quad (9)$$

where $y' = \bar{y} - M\bar{x} - N\tilde{z}$, with $\tilde{z} = \frac{1}{r} Z e_{r-1}$. This is the reduced system of observation equations for a single CORS platform equipped with multiple antennas.

3 Ambiguity resolution between CORS arrays

3.1 Ionosphere-weighted differential CORS array model

To determine the differential CORS array model for two CORS platforms equipped with multiple antennas, we can take the difference between their single CORS system of equations. For two CORS platforms, say b and u, having the reduced observations $\bar{y}_\mathrm{b}$ and $\bar{y}_\mathrm{u}$, the between-platform system of observation equations, therefore, reads

$$\mathsf{E}(y'_\mathrm{bu}) = (e_{2f} \otimes g_\mathrm{b})\tau_\mathrm{bu} + \nu \otimes \iota_\mathrm{bu} + Na_\mathrm{bu} \quad (10)$$

with $y'_\mathrm{bu} = \bar{y}_\mathrm{u} - \bar{y}_\mathrm{b} - M_\mathrm{u}\bar{x}_\mathrm{u} + M_\mathrm{b}\bar{x}_\mathrm{b} - N(\tilde{z}_\mathrm{u} - \tilde{z}_\mathrm{b})$, $\tau_\mathrm{bu} = \tau_\mathrm{u} - \tau_\mathrm{b}$ ($g_\mathrm{b} \approx g_\mathrm{u}$), and $a_\mathrm{bu} = a_{1;\mathrm{u}} - a_{1;\mathrm{b}}$. Note that a_bu is now again a DD *integer* ambiguity vector.

With the assumption that the same type of receivers are used on the two platforms (i.e. $Q_{f;\mathrm{b}} = Q_{f;\mathrm{u}} = Q_f$), the variance matrix of y'_bu is given as

$$\mathsf{D}(y'_\mathrm{bu}) = \frac{1}{r} Q_f \otimes W^{-1}, \quad W^{-1} = D_{s+1}^T Q_0 D_{s+1} \quad (11)$$

where $Q_0 = Q_{s;\mathrm{u}} + Q_{s;\mathrm{b}}$ is the cofactor matrix of the between-platform SD observations. This shows how between-platform parameter estimation can benefit from the antenna array and in particular from r, the number of antennas in the array.

The ionosphere-weighted version of (10) and (11) is obtained if we add the ionospheric pseudo-observation equations

$$\mathsf{E}(\iota^0_\mathrm{bu}) = \iota_\mathrm{bu}, \quad \mathsf{D}(\iota^0_\mathrm{bu}) = \sigma_\iota^2 \otimes W^{-1} \quad (12)$$

in which the variance σ_ι^2 is used to model the between-platform spatial uncertainty of the ionosphere, i.e. σ_ι^2 is small for short baselines and large for long baselines. The two extreme cases, $\sigma_\iota^2 = 0$ and $\sigma_\iota^2 = \infty$ are referred to as the ionosphere-fixed and ionosphere-float model, respectively.

3.2 Ionosphere-weighted CORS ambiguity resolution

If we use (12) to eliminate the unknown ionospheric delays from (10), the single-epoch ionosphere-weighted model may also be written as

$$\begin{aligned} \mathsf{E}(y) &= [e_{2f} \otimes g \;\; \Gamma \otimes I_s] \begin{bmatrix} \tau \\ a \end{bmatrix} \\ \mathsf{D}(y) &= \left(\tfrac{1}{r} Q_f + \sigma_\iota^2 \nu\nu^T\right) \otimes W^{-1} \end{aligned} \tag{13}$$

where $y = y'_{\mathrm{bu}} - \nu \otimes \iota^0_{\mathrm{bu}}$, $\Gamma = [\Lambda, 0]^T$. The short-hands g, τ and a have been used instead of g_{b}, τ_{bu} and a_{bu}. When we solve the ionosphere-weighted model for the multi-epoch case, we assume no time correlation between the observables and the ambiguity vector a to be time constant.

We now determine the multi-epoch ambiguity variance matrix for three different scenarios. In the first scenario, referred to as *geometry-fixed*, all the tropospheric delays are assumed known. The corresponding ambiguity variance matrix is given as

$$Q^{(\mathrm{fixed})}_{\hat{a}\hat{a}} = \frac{1}{r}\frac{1}{k}\left[\Lambda^{-1}(Q_\phi + \alpha\mu\mu^T)\Lambda^{-1}\right] \otimes \overline{W}^{-1} \tag{14}$$

with the time-average weight matrix $\overline{W} = \frac{1}{k}\sum_{t=1}^{k} W_t$ and ionosphere weighting scalar

$$\alpha = \left[(r\sigma_\iota^2)^{-1} + (\mu^T Q_p^{-1}\mu)\right]^{-1} \tag{15}$$

In the second scenario, referred to as *geometry-free*, all the slant tropospheric delays are assumed unknown. That is, no mapping is applied (i.e. g is replaced by I_s) and the delays are assumed to change over time. Referring to Appendix B, the corresponding ambiguity variance matrix is given as

$$Q^{(\mathrm{free})}_{\hat{a}\hat{a}} = Q^{(\mathrm{fixed})}_{\hat{a}\hat{a}} + \frac{1}{k} c^2_{\hat{\tau}_{\mathrm{free}}} qq^T \otimes \overline{W}^{-1} \tag{16}$$

with

$$\begin{aligned} q &= \Lambda^{-1}\left(I_f + \alpha\mu\mu^T Q_p^{-1}\right) e_f \\ c^2_{\hat{\tau}_{\mathrm{free}}} &= \left[e_f^T(\tfrac{1}{r}Q_p + \sigma_\iota^2\mu\mu^T)^{-1}e_f\right]^{-1} \end{aligned}$$

Finally, the third scenario, referred to as *geometry-based*, sits in between the geometry-fixed one and the geometry-free one. It is the scenario in which the ZTD is considered unknown, but constant in time. Referring to Appendix C, the corresponding ambiguity variance matrix is given as

$$Q_{\hat{a}\hat{a}} = Q^{(\mathrm{fixed})}_{\hat{a}\hat{a}} + \frac{1}{k} c^2_{\hat{\tau}} qq^T \otimes P_{\bar{g}} \overline{W}^{-1} \tag{17}$$

with $\bar{g} = \left(\sum_{t=1}^{k} W_t\right)^{-1}\left(\sum_{t=1}^{k} W_t g_t\right)$, the weighted average ZTD map, the orthogonal projector $P_{\bar{g}} = \bar{g}(\bar{g}^T\overline{W}\bar{g})^{-1}\bar{g}^T\overline{W}$, and

$$\begin{aligned} c^2_{\hat{\tau}} &= c^2_{\hat{\tau}_{\mathrm{free}}}\left[1 + \frac{c^2_{\hat{\tau}_{\mathrm{free}}}}{c^2_{\hat{\tau}|a}} \frac{\frac{1}{k}\sum_{t=1}^{k}(g_t-\bar{g})^T W_t (g_t-\bar{g})}{\bar{g}^T\overline{W}\bar{g}}\right]^{-1} \\ c^2_{\hat{\tau}|a} &= \left[e_{2f}^T(\tfrac{1}{r}Q_f + \sigma_\iota^2\nu\nu^T)^{-1}e_{2f}\right]^{-1} \end{aligned}$$

Note that $c^2_{\hat{\tau}} \le c^2_{\hat{\tau}_{\mathrm{free}}}$, with equality in the single-epoch case, and that $Q_{\hat{a}\hat{a}}$ and $Q^{(\mathrm{free})}_{\hat{a}\hat{a}}$ are a rank -1 update and a rank $-s$ update of $Q^{(\mathrm{fixed})}_{\hat{a}\hat{a}}$. Hence, in terms of the ambiguity precision, the three cases can be ordered as

$$Q^{(\mathrm{fixed})}_{\hat{a}\hat{a}} \le Q_{\hat{a}\hat{a}} \le Q^{(\mathrm{free})}_{\hat{a}\hat{a}} \tag{18}$$

The geometry-fixed model gives the most precise ambiguities, while the geometry-free model, being the weakest, gives the most imprecise ambiguities.

4 APPP-CORS simulation results

4.1 Simulation set-up

The APPP-CORS ambiguity resolution performance will be analyzed for different model settings with varying measurement scenarios. A GPS ephemerides almanac is used to simulate three baselines in the Perth area, Western Australia, for 24 h with a sampling interval of 1 s and a 10° cut-off elevation. An elevation-dependent weighting function is applied such that the observation variance at elevation θ is given as

$$\sigma^2(\theta) = \sigma_0^2 / \sin^2\theta$$

with σ_0 the observation standard deviation (STD) at zenith. Table 1 shows the σ_0 values of the reduced observations for 1, 4 and 9 antennas. Three settings of the a priori ionospheric STD are considered, namely $\sigma_\iota = 5$, 10 cm and ∞. These first two values correspond with baseline lengths of approximately 50 and 100 km (Schaffrin and Bock 1988; Odijk

Table 1 STDs at zenith of reduced undifferenced phase and code observations for different number of antennas (# ant)

# ant	σ_ϕ (mm)			σ_p (cm)		
	L1	L2	L5	P1	P2	P5
1	2	2	1.5	20	20	15
4	1	1	0.75	10	10	7.5
9	0.67	0.67	0.5	6.7	6.7	5

2000; Liu and Lachapelle 2002; Li et al 2013). The models with $\sigma_\iota = 0$ and $\sigma_\iota = \infty$ are referred to as the ionosphere-fixed and ionosphere-float model, respectively. Thus, in the latter model the ionospheric delays are estimated without constraint.

To study the full and partial ambiguity resolution (FAR and PAR) performances, their success rates and time to first fix (TTFF) are computed for different scenarios. Here, TTFF is defined as the number of epochs needed to achieve the user-defined success rate P_0. The simulation scenarios differ with respect to number of frequencies used, number of antennas used, value of a priori ionospheric STD and whether or not geometry is included in the design matrix.

For the success rate computation, we employ the Ps-LAMBDA software, a recently released Matlab toolbox, in which a variety of easy-to-use success rate approximations and bounds are implemented (Verhagen et al 2013). The software only needs the variance matrix of the float ambiguity solution as input. With Ps-LAMBDA one can compute the success rates of integer least-squares (ILS), integer bootstrapping (IB) and integer rounding (IR), see Verhagen and Li (2013).

In the present contribution, the IB success rate is used. It is a sharp lower bound of the ILS success rate and it is defined as (Teunissen 1998b),

$$\mathrm{P}(\check{z}_{\mathrm{IB}} = z) = \prod_{i=1}^{n} \left(2\Phi\left(\frac{1}{2\sigma_{\hat{z}_{i|I}}} \right) - 1 \right) \tag{19}$$

with $\Phi(x) = \int_{-\infty}^{x} \frac{1}{\sqrt{2\pi}} \exp\{-\frac{1}{2}v^2\}\mathrm{d}v$ and where $\sigma_{\hat{z}_{i|I}}$ is the STD of the ith decorrelated ambiguity, conditioned on the ambiguities $I = \{i+1, \ldots, n\}$.

4.2 Success rate performance of antenna array

4.2.1 Geometry-based single-epoch ambiguity success rates

We have computed the single-epoch success rate histograms for the dual- and triple-frequency geometry-based CORS model (13), using 1, 4 and 9 antennas per platform. The histograms are shown in Fig. 2 for $\sigma_\iota = 5$, 10 cm and ∞. The corresponding mean values of the success rate histograms are shown in Fig. 3.

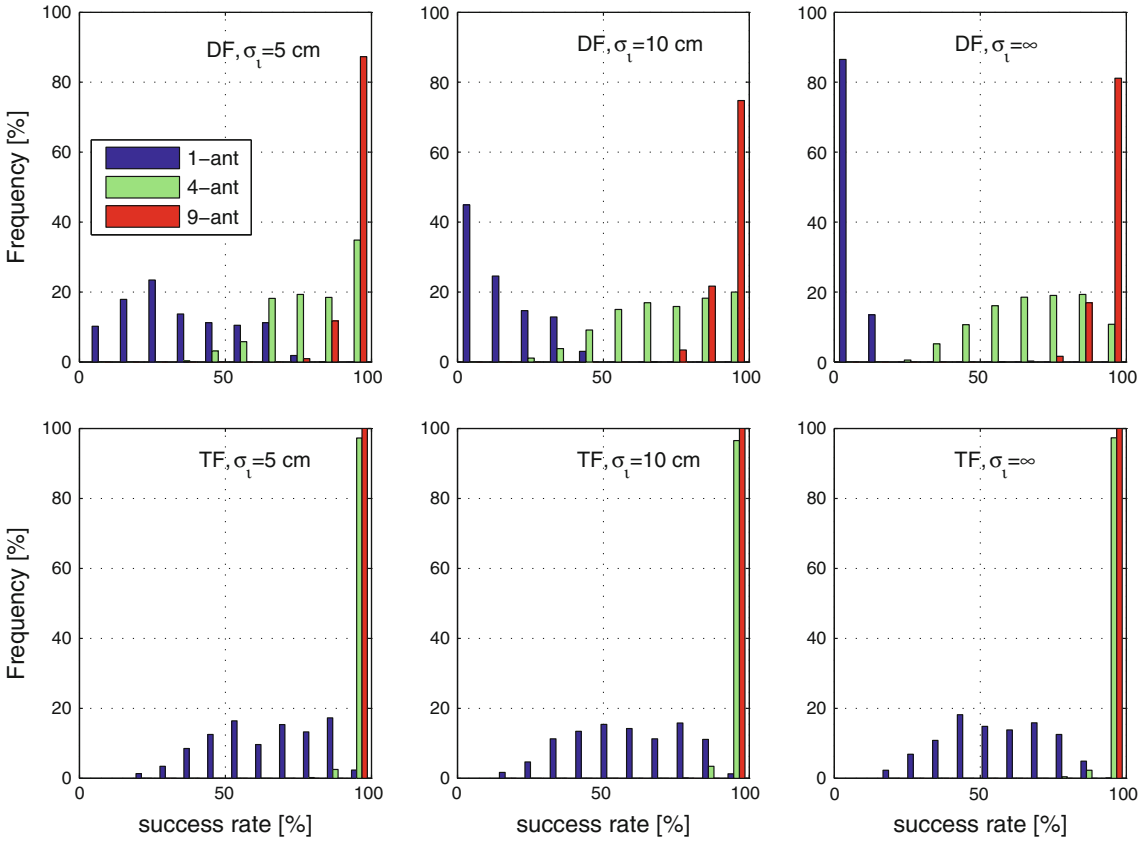

Fig. 2 Single-epoch success rate histograms for the dual-frequency (DF) and triple-frequency (TF) geometry-based CORS model (13), using 1 (*blue*), 4 (*green*) and 9 (*red*) antennas per platform. The histograms are shown for $\sigma_\iota = 5$, 10 cm and ∞

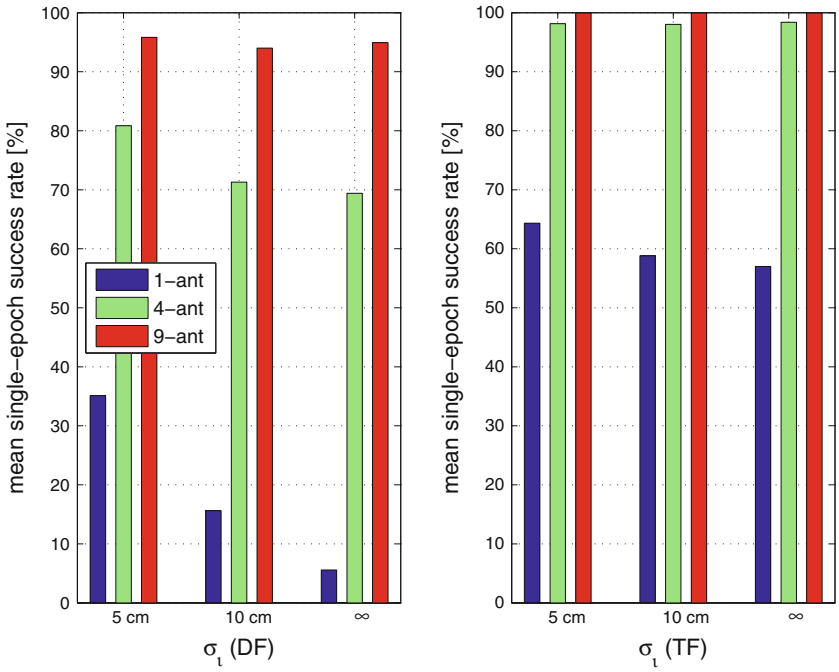

Fig. 3 The mean single-epoch success rates (%) of the histograms of Fig. 2

The superior performance of the nine-antenna platform is clearly visible. In general, the results show that single-epoch ambiguity resolution is almost impossible with a single antenna, but that it may become possible with four antennas and is almost always possible when using nine antennas.

We also note a clear difference in performance between the dual- and triple-frequency case. Compared to the triple-frequency model, the success rate improvements gained from using multiple antennas are more remarkable for the dual-frequency model. This is due to the fact that the triple-frequency model is stronger than its dual-frequency counterpart. The stronger the model, the more difficult it becomes in general to realize further improvements. Particularly note that the increase from 4 to 9 antennas shows only a slight improvement in the triple-frequency case.

Another difference between the dual- and triple-frequency cases is the success rate sensitivity for varying values of σ_ι. The dual-frequency results (*top row* of Fig. 2) show that the nine-antenna histograms are relatively insensitive to the varying values of σ_ι, whereas the other dual-frequency histograms, in particular those of the one-antenna case, change significantly for varying values of σ_ι. This sensitivity for varying σ_ι is much less pronounced in the triple-frequency case (*bottom row* of Fig. 2). Thus, as the model gets stronger (i.e. more antennas and/or more frequencies), the success rate sensitivity for varying σ_ι becomes less. This is also clear from the mean success rates given in Fig. 3. This is an important result as it shows that the multiple antenna performance, especially in the triple-frequency case, becomes to a large degree independent of baseline length. Thus with more antennas, the CORS baseline lengths can be extended, thereby allowing fewer stations per unit of area.

Table 2 Mean single-epoch success rates (%) of the geometry-fixed APPP-CORS (ZTD known)

σ_ι (cm)	Number of antennas					
	1		4		9	
	DF	TF	DF	TF	DF	TF
5	96.5	99.4	100.0	100.0	100.0	100.0
10	80.9	98.4	99.7	100.0	100.0	100.0
∞	25.9	96.0	97.8	100.0	100.0	100.0

4.2.2 Geometry-fixed single-epoch ambiguity success rates

The geometry-fixed model refers to the CORS model (13) with the ZTD parameter assumed known. Hence, this model applies to the case when the baseline is so short that the relative tropospheric delays may be assumed absent. Since the geometry-fixed model is the strongest CORS model, the single-epoch success rates are generally very high as shown in Table 2.

4.2.3 Geometry-free multi-epoch ambiguity success rates

The geometry-free model refers to the CORS model (13), but now with the mapped tropospheric zenith delay replaced with the unknown *slant* tropospheric delay. Hence, the unknown DD slant tropospheric delay is estimated without the use of

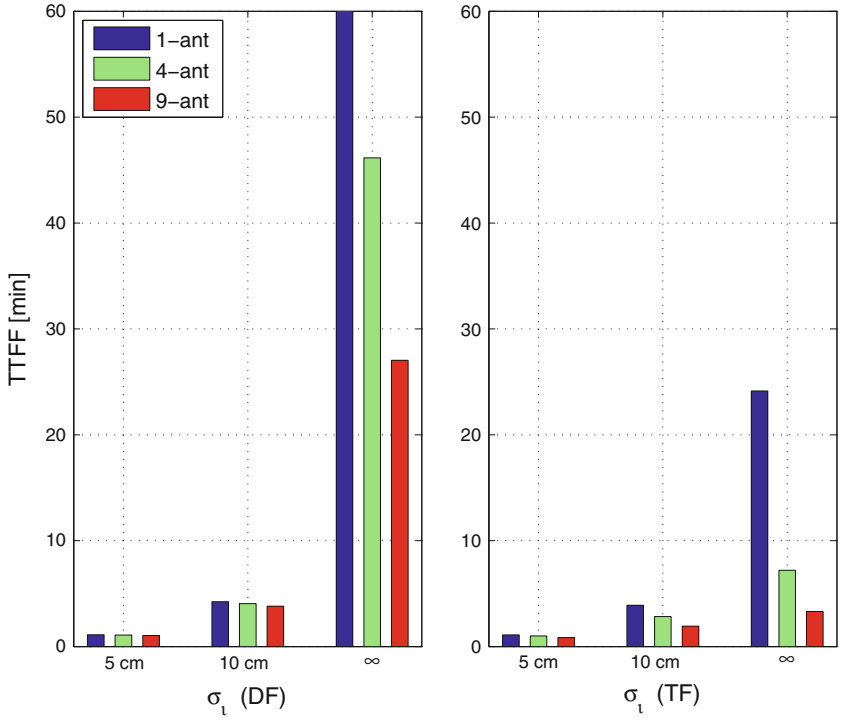

Fig. 4 Mean TTFF for successful ambiguity resolution ($P_0 = 99.9\ \%$) of the geometry-free APPP-CORS model (slant tropospheric delays unknown)

a mapping function and geometry. This model is, therefore, a very weak model when compared to the previous two. As instantaneous ambiguity resolution is impossible, we analyze its TTFF using $P_0 = 99.9\ \%$ as the pre-defined required success rate. For each scenario, we start the computation every 2 min for 24 h, such that 720 TTFFs in total are obtained. The mean TTFFs of these scenarios are shown in Fig. 4.

The results show that the nine-antenna, triple-frequency, geometry-free TTFF can be kept below 4 min in all cases, but that this is true for the dual-frequency case only for $\sigma_\iota \leq 10$ cm. Again we note that the improvements due to increase in number of antennas are largest for the weakest model ($\sigma_\iota = \infty$).

4.3 Partial ambiguity resolution

4.3.1 Success rate fluctuations

The results presented in the previous sections are all based on FAR, i.e. the resolution of the complete vector of integer ambiguities. FAR success rates, however, may sometimes exhibit rapid fluctuations, thus for instance having FAR being successful in one instance, while unsuccessful in another close by instance. This can be explained as follows. As the receiver-satellite geometry changes over time, the single-epoch FAR success rates will of course also change over time. This change over time will be rather smooth as long as the same satellites are tracked. However, if a change in number of tracked satellites occurs, it is not so. Such rapid fluctuations are shown in Fig. 5 (*red curve*).

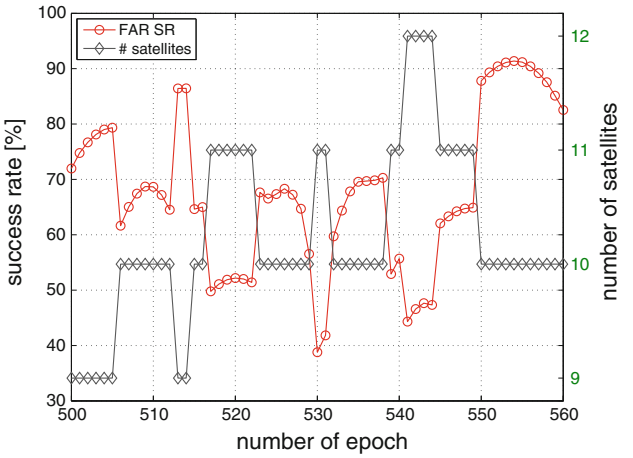

Fig. 5 Single-epoch FAR success rates for the four-antenna, dual-frequency geometry-based APPP-CORS model (13) with $\sigma_\iota = 5$ cm. The epoch numbers 500 and 560 correspond to the GPS times 16:40 and 18:40

These fluctuations are due to the rising and setting of satellites. Since satellites that rise or set have small elevations, their carrier phase and code data receive low weights in the adjustment process, thus resulting in a relative poor precision of the corresponding single-epoch estimated ambiguities. Since FAR tries to resolve the complete ambiguity vector and thus includes these poorly determined ambiguities by definition, the FAR success rates suffer from their poor precision.

This effect of rising and setting satellites is clearly visible in Fig. 5. It shows that when the number of satellites

increases (i.e. when the ambiguities of a low elevation satellite are included), the FAR success rates drop dramatically. Similarly, when the number of satellites decreases (i.e. when the ambiguities of a low elevation satellites are excluded), we see a dramatic increase in the FAR success rates.

4.3.2 PAR implementation

Partial ambiguity resolution is a flexible method that allows one to combat such rapid success rate fluctuations. Instead of aiming to always resolve the complete ambiguity vector, which results in fluctuating FAR success rates, PAR allows the subsets of ambiguities to be resolved, thereby enabling the realization of more stable success rates. The PAR concept was introduced in Teunissen et al (1999). Since then various variations on the PAR concept were proposed in the literature, see e.g. (Mowlam 2004; Dai et al 2007; Lawrence 2009; Takasu and Yasuda 2010; Pantoja 2009; Parkins 2011). Several of these variations use the satellite elevation as criterion for inclusion or exclusion of the ambiguities. However, since it is the ambiguity precision that ultimately determines the success rate, and not the satellite elevation per se, we will be using the PAR method of Teunissen et al (1999). The method is implemented in the extended version of the LAMBDA software (Verhagen and Li 2012).

The method works with decorrelated (i.e. Z-transformed) ambiguities and it can be described briefly as follows. Let $n-k$ be the largest range for which the inequality

$$\prod_{i=k+1}^{n}\left(2\Phi\left(\frac{1}{2\sigma_{\hat{z}_{i|I}}}\right)-1\right)\geq P_0 \tag{20}$$

holds true, where P_0 is the user-defined smallest value of an acceptable success rate and $\sigma_{\hat{z}_{i|I}}$ is the STD of the ith ambiguity conditioned on the ambiguities $I=\{i+1,\ldots,n\}$. Once k and, therefore, $\hat{z}_{\mathrm{PAR}}=[\hat{z}_{k+1},\ldots,\hat{z}_n]^T$, with variance matrix $Q_{\hat{z}_{\mathrm{PAR}}\hat{z}_{\mathrm{PAR}}}$ have been determined, the integer solution $\check{z}_{\mathrm{PAR}}$ is obtained using the LAMBDA method.

4.3.3 PAR and FAR illustrated

To illustrate the workings of PAR versus FAR, we applied PAR to the single-epoch triple-frequency four-antenna geometry-based model, with $\sigma_\iota=5$ cm, during a period where the FAR success rates show clear fluctuations (see Fig. 6). The user-defined minimal success rate was set to $P_0=99.9\,\%$.

As the results of Fig. 6 shown, the FAR success rates (*red curve with circles*) fluctuate, whereas those of PAR (*green curve with squares*) stay quite stable. FAR starts successfully at epoch 400 (red and green curves coincide, i.e. all ambiguities are resolved), but then drops dramatically due to the inclusion of more ambiguities from a rising new satellite. From then on, the FAR success rates keep changing over time, but remain, for quite some time, too small to be acceptable. They only become acceptable again in the short periods of epoch 422–426 and 434–438 (red and green curves coincide). Thus apart from these few epochs, FAR is unsuccessful over the complete period of epoch 400–450. PAR, on the other hand, achieves that ambiguities get resolved during the whole period, thus enabling the user to benefit from the improvements this brings.

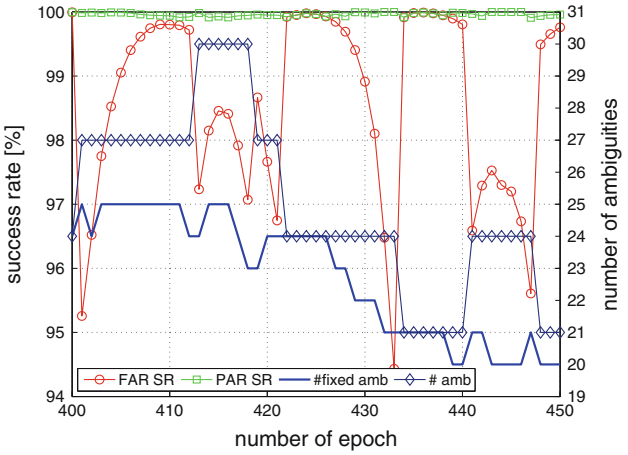

Fig. 6 A comparison between single-epoch, triple-frequency FAR and PAR success rates (SR) based on the 4-antenna geometry-based model, with $\sigma_\iota=5$ cm. The total number of ambiguities and the PAR fixed number of ambiguities (*blue curve*) are also shown; the epoch numbers 400 and 450 correspond to GPS times 13:20 and 15:00

4.3.4 PAR benefits

Ambiguity resolution is not a goal in itself. The purpose of ambiguity resolution is to be able to improve the precision of the estimated parameters one is interested in. In case of our CORS model, we take those parameters to be the DD slant ionospheric delays. We base our scalar measure of the precision of the estimated DD slant ionospheric delays on the determinant of their variance matrix. We, therefore, define this measure as

$$\bar{\sigma}_\iota=\sqrt{\det(Q_{\check{\iota}\check{\iota}})}^{\frac{1}{q}}$$

with $Q_{\check{\iota}\check{\iota}}$ the $q\times q$ variance matrix of the PAR-based, estimated q DD ionospheric delays. The measure $\bar{\sigma}_\iota$ can be interpreted as a (geometric) average of the ionospheric precision. Furthermore, since this measure is based on the determinant of the variance matrix, it can also be related to the volume of the confidence ellipsoid of the estimated ionospheric delays.

We will now study the capabilities of PAR in improving the precision of the estimated ionospheric delays. We do this by analyzing how long it takes for PAR to bring $\bar{\sigma}_\iota$ down to a value smaller than a pre-set criterion, i.e. $\bar{\sigma}_\iota\leq\sigma_\iota^0$ (we consider the two cases: $\sigma_\iota^0=1$ and 2 cm). This conditioned PAR

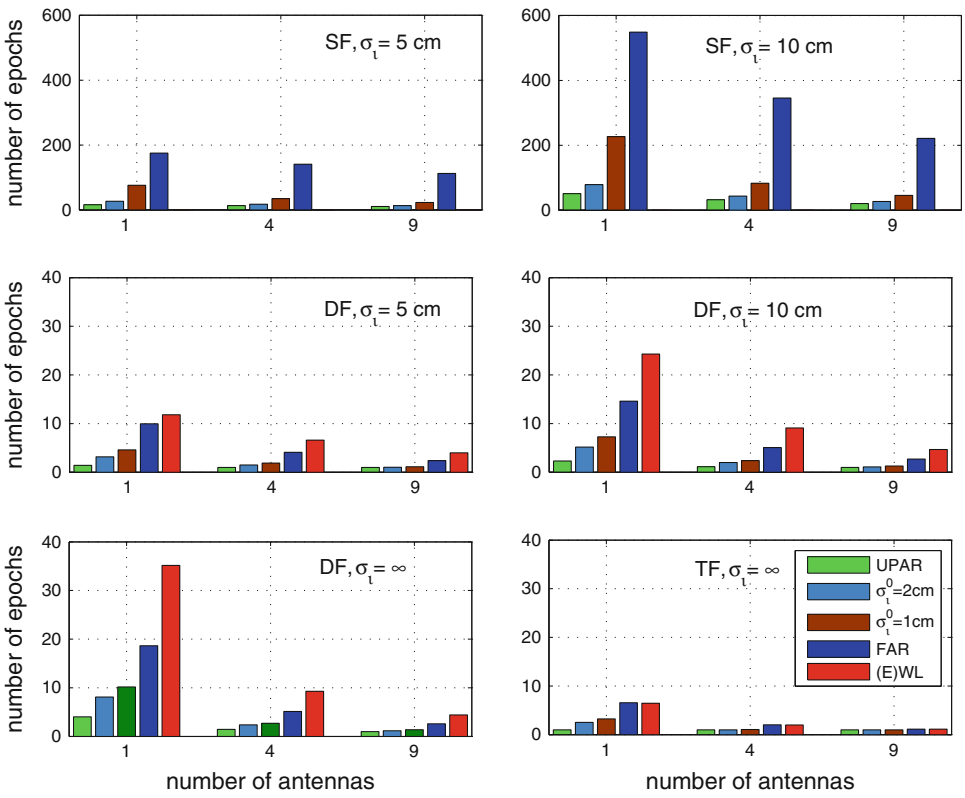

Fig. 7 Mean number of epochs needed to realize with the geometry-based CORS model (13), unconditioned PAR (UPAR), conditioned PAR (CPAR, $\sigma_\iota^0 = 2$, 1 cm), FAR, dual-frequency widelane (WL) ambiguity resolution or triple-frequency extra-widelane (EWL) ambiguity resolution

(CPAR) will be compared with FAR and with PAR without the condition on $\bar{\sigma}_\iota$. The latter is referred to as unconditioned PAR (UPAR).

The analyses are done for the geometry-based CORS model (13) with different settings. Per scenario the computations are repeated every 2 min for 24 h, giving a total of 720 outcomes, of which the mean is computed and shown in Fig. 7. The results are shown for the single-, dual- and triple-frequency case, using $\sigma_\iota = 5$, 10 cm and ∞. The triple-frequency cases with $\sigma_\iota = 5$ and 10 cm, and the single-frequency case with $\sigma_\iota = \infty$ are excluded. The first two cases are excluded, since FAR is already fast enough for those cases. The third case is excluded, because its UPAR takes too long to be distinguished from FAR and CPAR.

The results are shown in Fig. 7. The number of epochs needed to fulfill the different criteria depends on the model strength. The more frequencies, the more antennas and the smaller the a priori ionospheric STD, the fewer epochs are needed. As the results show, there is particularly a significant difference in performance between the single-frequency case (*first row* of Fig. 7) and the dual-frequency case.

Also note, although FAR improves significantly by adding antennas, it still can take quite some time for some cases, in particular for the single-frequency scenarios. In contrast, UPAR is mostly very fast. Furthermore, the number of epochs needed for PAR to improve the ionospheric precision to better than 2 or 1 cm is less than what is needed for FAR. Especially with more antennas, conditioned PAR can be surprisingly fast and sometimes even instantaneous.

4.4 What about widelaning?

Widelaning is still a popular technique for ambiguity resolution, see e.g. (Hernández-Pajares et al 2003; Isshiki 2004; Werner and Winkel 2003; Richert and El-Sheimy 2007; Cocard et al 2008; Feng 2008; Li et al 2010). The common rationale behind using widelane combinations is that their ambiguities, due to the longer wavelengths, can be resolved better than the original ambiguities (Melbourne 1985; Blewitt 1989; Dong and Bock 1989; Wübbena 1991; Cocard and Geiger 1992; Goad 1992; Euler and Landau 1992).

Widelaning, however, has its limitations, and moreover, it is also not explicitly needed. As is shown in Teunissen (1997), the widelaning technique is as initialization automatically embedded in the LAMBDA method. Furthermore, with its automatic construction of the optimal decorrelating ambiguity transformation, the LAMBDA method will then further improve upon the results achieved with the widelane (Teunissen et al 1997).

The limitations of the widelaning technique come even more to the fore if one considers models other than the geometry-free model, such as the geometry-based model, in which the relative receiver-satellite geometry is explicitly

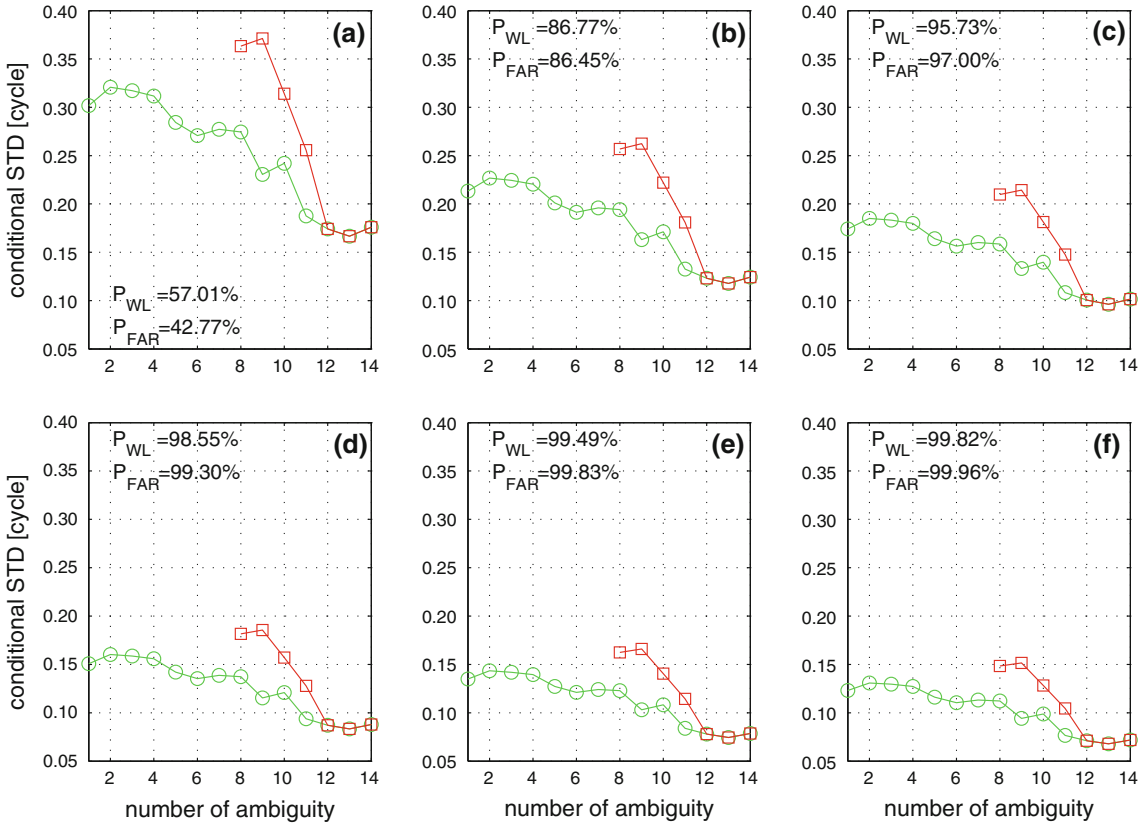

Fig. 8 Conditional STDs of all ambiguities ($Q_{\hat{a}\hat{a}}$) and WL ambiguities ($Q_{\hat{a}_w\hat{a}_w}$) after decorrelation based on the dual-frequency *geometry-based* model with $\sigma_\iota = 5$ cm. The subplots from (**a**) to (**f**) denote the results with the number of data epochs from 1 to 6

taken into account. Firstly, the widelaning technique requires the presence of multi-frequency data and does, therefore, not apply to single-frequency models. Secondly, the widelaning technique does not have the capability to take the impact of the receiver-satellite geometry on the ambiguity variance matrix into account. Both these limitations are absent with the LAMBDA method.

To study the widelaning performance for our geometry-based array model, we have included in Fig. 7 for the dual- and triple-frequency case, the performance of resolving the widelane L1–L2 (WL) and the (extra) widelanes L2–L5 and L1–L2 (EWL), respectively. By restricting attention to the widelane ambiguities only and thus not resolving the complete set of ambiguities, the widelaning approach is essentially an alternative PAR scheme (Teunissen et al 2002; Li et al 2010). If

$$Q_{\hat{a}\hat{a}} = \begin{bmatrix} Q_{11} & Q_{12} \\ Q_{21} & Q_{22} \end{bmatrix} \tag{21}$$

denotes the dual-frequency ambiguity variance matrix, with Q_{11} and Q_{22} the corresponding variance matrices of the L1 and L2 ambiguities, then the widelane ambiguity variance matrix is given as

$$Q_{\hat{a}_w\hat{a}_w} = Q_{11} - Q_{12} - Q_{21} + Q_{22} \tag{22}$$

This matrix is thus used to determine the ambiguity resolution performance for widelaning. The approach for the triple-frequency extra widelaning goes in a similar way.

The results of Fig. 7 show that in the triple-frequency case the number of epochs for PAR fixing of the EWL ambiguities is comparable with that for FAR. However, in the dual-frequency case the PAR fixing of the WL ambiguities is slower than FAR. Thus here widelaning performs even poorer than when resolving all ambiguities (FAR).

This can be explained by the above mentioned fact that widelaning does not take full advantage of the available information. To illustrate this in the present case, consider Fig. 8. The panels in this figure show a *red* and a *green* curve. The green curve gives the conditional STDs of the decorrelated ambiguities based on the original L1/L2 variance matrix $Q_{\hat{a}\hat{a}}$, whereas the red curve provides the conditional STDs of the decorrelated ambiguities based on the widelane variance matrix $Q_{\hat{a}_w\hat{a}_w}$. Eight satellites were tracked, thus giving $7 \times 2 = 14$ conditional STDs for the green curve and $\frac{1}{2} \times 14 = 7$ conditional STDs for the red curve. We note that in all six cases of Fig. 8, the red curve does not get below the

green curve. Hence, the decorrelated conditional STDs for widelaning are never smaller than their decorrelated L1/L2 counterparts. This immediately implies that in all six cases, the WL success rate is smaller than the PAR success rate of resolving the seven ambiguities $z_8, \ldots, z_{14}$. But even the FAR success rate is sometimes larger than the WL success rate (see last four panels of Fig. 8). Thus in those cases, even resolving all 14 ambiguities has a higher success rate than resolving the seven decorrelated WL ambiguities.

5 Conclusions

A-PPP is a measurement concept that uses GNSS data, from multiple antennas in an array of known geometry, to realize improved GNSS parameter estimation. In this contribution, we applied the A-PPP concept and studied the benefits of array-aided CORS ambiguity resolution. The mathematical model was formulated to show how the platform-array data can be reduced and how the variance matrix of the between-platform ambiguities can profit from the increased precision of the reduced platform data. The ambiguity resolution performance was demonstrated for varying scenarios using simulation. For three different models, geometry-fixed, geometry-based and geometry-float, the ambiguity success rates were analyzed with varying the number of frequencies, the number of antennas and the weight of the ionospheric constraints.

It was demonstrated that significant gains can be expected when the stations are equipped with antenna arrays; in some important cases even enabling instantaneous ambiguity resolution. It was also shown that as the model gets stronger (i.e. more antennas and/or more frequencies), the success rate sensitivity for varying σ_ι becomes less. As a consequence, the multiple antenna performance, especially in the triple-frequency case, becomes to a large degree independent of baseline length. Thus with more antennas, the CORS baseline lengths can be extended, thereby allowing fewer stations per unit of area.

We also compared PAR with FAR, together with the impact it has on improving the precision of the estimated ionospheric delays. It was shown that PAR needs less time than FAR to improve the ionospheric precision to better than a few centimetres. Especially with more antennas, conditioned PAR can be very fast and sometimes even instantaneous. In addition, we illustrated and explained the limitations when using widelaning.

Note: The LAMBDA and Ps-LAMBDA softwares used in this study can be freely downloaded from http://gnss.curtin.edu.au.

Acknowledgments This work has been executed in the framework of the Positioning Program Project 1.01 'New carrier phase processing strategies for achieving precise and reliable multi-satellite, multi-frequency GNSS/RNSS positioning in Australia' of the Cooperative Research Centre for Spatial Information. PJG Teunissen is the recipient of an Australian Research Council (ARC) Federation Fellowship (FF0883188). This support is gratefully acknowledged. This work is also supported by the National Natural Science Funds of China (41374031), the State Key Laboratory of Geo-information Engineering (SKLGIE2013-M-2-2) and the Key Laboratory of Geo-informatics of State Bureau of Surveying and Mapping (201306).

Appendix

Assuming all matrices and vectors involved have appropriate dimensions, the following properties of the Kronecker product $\otimes$ and vectorization operator $\mathtt{vec}$ (Rao 1973):

$$(AB) \otimes (CD) = (A \otimes C)(B \otimes D) \tag{23}$$

$$\mathtt{vec}(ABC) = (C^T \otimes A)\mathtt{vec}(B) \tag{24}$$

and the projector identity (Teunissen 2003)

$$QD_r(D_r^T Q D_r)^{-1} D_r^T = I_r - e_r(e_r^T Q^{-1} e_r)^{-1} e_r^T Q^{-1} \tag{25}$$

with $D_r^T e_r = 0$, will be frequently applied in the derivations.

Appendix A: Derivation of some formulae in Sect. 2

To derive (5), we apply the error propagation law to

$$\begin{bmatrix} y_1 \\ \mathtt{vec}(\tilde{Y}) \end{bmatrix} = \mathtt{vec}(Y R_r) = (R_r^T \otimes I_{2fs})\mathtt{vec}(Y) \tag{26}$$

where $R_r = [c_1, D_r]$. This gives

$$\begin{aligned} \mathsf{D}\begin{bmatrix} y_1 \\ \mathtt{vec}(\tilde{Y}) \end{bmatrix} &= (R_r^T \otimes I_{2fs})\mathsf{D}(\mathtt{vec}(Y))(R_r \otimes I_{2fs}) \\ &= (R_r^T \otimes I_{2fs})(Q_r \otimes Q)(R_r \otimes I_{2fs}) \\ &= \begin{bmatrix} c_1^T Q_r c_1 & c_1^T Q_r D_r \\ D_r^T Q_r c_1 & D_r^T Q_r D_r \end{bmatrix} \otimes Q \end{aligned} \tag{27}$$

To derive the first equation of (8), we apply the invertible transformation (6) to (3). It follows:

$$\begin{aligned} &\left[\left(1, \; -c_1^T Q_r D_r (D_r^T Q_r D_r)^{-1}\right) \otimes I_{2fs}\right] \begin{bmatrix} y_1 \\ \mathtt{vec}(\tilde{Y}) \end{bmatrix} \\ &= y_1 - (c_1^T Q_r D_r (D_r^T Q_r D_r)^{-1} \otimes I_{2fs})\mathtt{vec}(\tilde{Y}) \\ &= y_1 - \mathtt{vec}(\tilde{Y}(D_r^T Q_r D_r)^{-1} D_r^T Q_r c_1) \\ &= y_1 - Y D_r (D_r^T Q_r D_r)^{-1} D_r^T Q_r c_1 \\ &= y_1 - Y\left[I_r - Q_r^{-1} e_r (e_r^T Q_r^{-1} e_r)^{-1} e_r^T\right] c_1 \\ &= Y Q_r^{-1} e_r (e_r^T Q_r^{-1} e_r)^{-1} \end{aligned} \tag{28}$$

where the identity (25) was applied. One can easily work out the variance matrix (8) using this identity.

Appendix B: Derivation of variance matrix (16)

For the geometry-free model, we replace g with I_s in (13) and further use the differencing matrix $D_{2f}^T \otimes I_s$ to eliminate troposphere design matrix:

$$[D_{2f}^T \Gamma \otimes I_s] \text{ and } D_{2f}^T \tilde{Q} D_{2f} \otimes W^{-1} \tag{29}$$

with $\tilde{Q} = \frac{1}{r} Q_f + \sigma_\iota^2 \nu\nu^T$. This gives the normal matrix of k epochs for ambiguities as

$$\left(\Gamma^T D_{2f} (D_{2f}^T \tilde{Q} D_{2f})^{-1} D_{2f}^T \Gamma\right) \otimes (k\overline{W}) = \tilde{N} \otimes (k\overline{W}) \tag{30}$$

We now concentrate on the first part $\tilde{N}$ only and use the identity (25) to rewrite it as

$$\tilde{N} = \Gamma^T \tilde{Q}^{-1} \Gamma - \Gamma^T \tilde{Q}^{-1} e_{2f} (e_{2f}^T \tilde{Q}^{-1} e_{2f})^{-1} e_{2f}^T \tilde{Q}^{-1} \Gamma \tag{31}$$

Using matrix inversion lemma gives:

$$\tilde{N}^{-1} = (\Gamma^T \tilde{Q}^{-1} \Gamma)^{-1} + c_{\hat{\tau}_{\text{free}}}^2 q q^T \tag{32}$$

with

$$c_{\hat{\tau}_{\text{free}}}^{-2} = e_{2f}^T \tilde{Q}^{-1} e_{2f} - e_{2f}^T \tilde{Q}^{-1} (\Gamma^T \tilde{Q}^{-1} \Gamma)^{-1} \Gamma^T \tilde{Q}^{-1} e_{2f} \tag{33}$$

$$q = (\Gamma^T \tilde{Q}^{-1} \Gamma)^{-1} \Gamma^T \tilde{Q}^{-1} e_{2f} \tag{34}$$

We first work out $c_{\hat{\tau}_{\text{free}}}^{-2}$. Using the analogous projector identity

$$I_{2f} - \Gamma (\Gamma^T \tilde{Q}^{-1} \Gamma)^{-1} \Gamma^T \tilde{Q}^{-1} = \tilde{Q} \Gamma_\perp (\Gamma_\perp^T \tilde{Q} \Gamma_\perp)^{-1} \Gamma_\perp^T \tag{35}$$

with $\Gamma_\perp = [0,\ I_f]^T$, we get

$$\begin{aligned} c_{\hat{\tau}_{\text{free}}}^{-2} &= e_{2f}^T \Gamma_\perp (\Gamma_\perp^T \tilde{Q} \Gamma_\perp)^{-1} \Gamma_\perp^T e_{2f} \\ &= e_f^T \left(\frac{1}{r} Q_p + \sigma_\iota^2 \mu\mu^T\right)^{-1} e_f \end{aligned}$$

where use is made of $\tilde{Q} = \frac{1}{r} Q_f + \sigma_\iota^2 \nu\nu^T$.

Now we work out the expression for q. Premultiplying the matrix identity (35) with $(\Gamma^T \Gamma)^{-1} \Gamma^T$ gives

$$\begin{aligned} &(\Gamma^T \tilde{Q}^{-1} \Gamma)^{-1} \Gamma^T \tilde{Q}^{-1} \\ &= (\Gamma^T \Gamma)^{-1} \Gamma^T \left(I_{2f} - \tilde{Q} \Gamma_\perp (\Gamma_\perp^T \tilde{Q} \Gamma_\perp)^{-1} \Gamma_\perp^T\right) \\ &= \Lambda^{-1} [I_f, 0] \left(I_{2f} - \tilde{Q} \begin{bmatrix} 0 \\ I_f \end{bmatrix} \left(\frac{1}{r} Q_p + \sigma_\iota^2 \mu\mu^T\right)^{-1} [0, I_f]\right) \end{aligned} \tag{36}$$

Hence

$$\begin{aligned} q &= (\Gamma^T \tilde{Q}^{-1} \Gamma)^{-1} \Gamma^T \tilde{Q}^{-1} e_{2f} \\ &= \Lambda^{-1} \left(e_f + \sigma_\iota^2 \mu\mu^T \left(\frac{1}{r} Q_p + \sigma_\iota^2 \mu\mu^T\right)^{-1} e_f\right) \end{aligned} \tag{37}$$

It is not difficult to verify that

$$I_f + \sigma_\iota^2 \mu\mu^T \left(\frac{1}{r} Q_p + \sigma_\iota^2 \mu\mu^T\right)^{-1} = I_f + \alpha \mu\mu^T Q_p^{-1}$$

with $\alpha = [(r\sigma_\iota^2)^{-1} + \mu^T Q_p^{-1} \mu]^{-1}$. Hence, for q we find

$$q = \Lambda^{-1} (I_f + \alpha \mu\mu^T Q_p^{-1}) e_f \tag{38}$$

It is rather easy to prove:

$$(\Gamma^T \tilde{Q}^{-1} \Gamma)^{-1} \otimes \frac{1}{k} \overline{W}^{-1} = Q_{\hat{a}\hat{a}}^{(\text{fixed})} \tag{39}$$

Finally, combining (30), (32) and (39) yields (16).

Appendix C: Derivation of variance matrix (17)

To specify the time variation of troposphere design matrix g and elevation-dependent weight matrix, we assign the epoch index t to g and W. The normal matrix of k epochs reads

$$\begin{bmatrix} (\Gamma^T \tilde{Q}^{-1} \Gamma) \otimes k\overline{W} & (\Gamma^T \tilde{Q}^{-1} e_{2f}) \otimes k\overline{W}\bar{g} \\ (e_{2f}^T \tilde{Q}^{-1} \Gamma) \otimes k\bar{g}^T \overline{W} & c_{\hat{\tau}|a}^{-2} \sum_{t=1}^k g_t^T W_t g_t \end{bmatrix} \tag{40}$$

with $\overline{W} = \frac{1}{k} \sum_{t=1}^k W_t$, $\bar{g} = \left(\sum_{t=1}^k W_t\right)^{-1} \sum_{t=1}^k W_t g_t$, $\sum_{t=1}^k W_t g_t = k\overline{W}\bar{g}$ and

$$c_{\hat{\tau}|a}^{-2} = e_{2f}^T \tilde{Q}^{-1} e_{2f} = e_{2f}^T \left(\frac{1}{r} Q_f + \sigma_\iota^2 \nu\nu^T\right)^{-1} e_{2f} \tag{41}$$

Reducing the ZTD parameter, the normal matrix of ambiguities over k epochs is

$$\left(Q_{\hat{a}\hat{a}}^{(\text{fixed})}\right)^{-1} - \frac{(\Gamma^T \tilde{Q}^{-1} e_{2f} \otimes \overline{W}\bar{g})(e_{2f}^T \tilde{Q}^{-1} \Gamma \otimes \bar{g}^T \overline{W})}{k^{-2} c_{\hat{\tau}|a}^{-2} \sum_{t=1}^k g_t^T W_t g_t} \tag{42}$$

Using the matrix inversion lemma, we obtain the variance matrix (43) of ambiguities.

$$Q_{\hat{a}\hat{a}} = Q_{\hat{a}\hat{a}}^{(\text{fixed})} + \frac{k^2 c_{\hat{\tau}|a}^2 Q_{\hat{a}\hat{a}}^{(\text{fixed})} (\Gamma^T \tilde{Q}^{-1} e_{2f} e_{2f}^T \tilde{Q}^{-1} \Gamma \otimes \overline{W}\bar{g}\bar{g}^T \overline{W}) Q_{\hat{a}\hat{a}}^{(\text{fixed})}}{\sum_{t=1}^k g_t^T W_t g_t - (e_{2f}^T \tilde{Q}^{-1} \Gamma \otimes \bar{g}^T \overline{W}) Q_{\hat{a}\hat{a}}^{(\text{fixed})} (\Gamma^T \tilde{Q}^{-1} e_{2f} \otimes \overline{W}\bar{g}) k^2 c_{\hat{\tau}|a}^2} = Q_{\hat{a}\hat{a}}^{(\text{fixed})} + \frac{U}{v} \tag{43}$$

Let us now focus on the fraction U/v of the second term only. We first simplify its numerator U. Substituting (39) into it yields:

$$\begin{aligned} U &= c^2_{\hat{\tau}|a} \underbrace{(\Gamma^T \tilde{Q}^{-1}\Gamma)^{-1}\Gamma^T \tilde{Q}^{-1} e_{2f}}_{q} \\ &\quad \times \underbrace{e^T_{2f} \tilde{Q}^{-1}\Gamma(\Gamma^T \tilde{Q}^{-1}\Gamma)^{-1}}_{q^T} \otimes \bar{g}\bar{g}^T \\ &= c^2_{\hat{\tau}|a} qq^T \otimes \bar{g}\bar{g}^T \end{aligned} \tag{44}$$

Substituting (39) into the denominator v of fraction yields:

$$\begin{aligned} v &= \sum_{t=1}^{k} g_t^T W_t g_t - \frac{k}{c^{-2}_{\hat{\tau}|a}} e^T_{2f} \tilde{Q}^{-1}\Gamma(\Gamma^T \tilde{Q}^{-1}\Gamma)^{-1} \\ &\quad \times \Gamma^T \tilde{Q}^{-1} e_{2f} \bar{g}^T \overline{W} \bar{g} \end{aligned} \tag{45}$$

$$= \sum_{t=1}^{k} g_t^T W_t g_t - \frac{k}{c^{-2}_{\hat{\tau}|a}} \left(c^{-2}_{\hat{\tau}|a} - c^{-2}_{\hat{\tau}_{\text{free}}} \right) \bar{g}^T \overline{W} \bar{g} \tag{46}$$

where use is made of (33) and (41). Further substituting the identity

$$\sum_{t=1}^{k} (g_t^T W_t g_t) = \sum_{t=1}^{k} (g_t - \bar{g})^T W_t (g_t - \bar{g}) + k \bar{g}^T \overline{W} \bar{g} \tag{47}$$

into (46) gives

$$v = \sum_{t=1}^{k} (g_t - \bar{g})^T W_t (g_t - \bar{g}) + k \frac{c^2_{\hat{\tau}|a}}{c^2_{\hat{\tau}_{\text{free}}}} \bar{g}^T \overline{W} \bar{g} \tag{48}$$

Therefore,

$$\frac{U}{v} = \frac{1}{k} c^2_{\hat{\tau}} qq^T \otimes P_{\bar{g}} \overline{W}^{-1} \tag{49}$$

where

$$c^2_{\hat{\tau}} = c^2_{\hat{\tau}_{\text{free}}} \left[1 + \frac{c^2_{\hat{\tau}_{\text{free}}}}{c^2_{\hat{\tau}|a}} \frac{\sum_{t=1}^{k} (g_t - \bar{g})^T W_t (g_t - \bar{g})}{k \bar{g}^T \overline{W} \bar{g}} \right]^{-1}$$

$$P_{\bar{g}} = \bar{g} (\bar{g}^T \overline{W} \bar{g})^{-1} \bar{g}^T \overline{W}$$

Finally, inserting (49) into (43) yields (17).

References

Blewitt G (1989) Carrier phase ambiguity resolution for the global positioning system applied to geodetic baselines up to 2000 km. J Geophys Res 94:135–151

Cocard C, Geiger A (1992) Systematic search for all possible widelanes. In: 6th International Geodetic Symposium on Satellite Positioning. Columbus, Ohio, pp 373–386

Cocard M, Bourgon S, Kamali O, Collins P (2008) A systematic investigation of optimal carrier-phase combinations for modernized triple-frequency GPS. J Geod 82(9):555–564

Dai L, Eslinger D, Sharpe T (2007) Innovative algorithms to improve long range RTK reliability and availability. In: ION NTM 2007, San Diego CA, pp 860–872.

Dong D, Bock Y (1989) Global Positioning System network analysis with phase ambiguity resolution applied to crustal deformation studies in California. J Geophys Res 94(B4):3949–3966

Euler H, Landau H (1992) Fast GPS ambiguity resolution on-the-fly for real-time applications. In: 6th International Geodetic Symposium on Satellite Positioning. Columbus, Ohio, pp 650–659

Feng Y (2008) GNSS three carrier ambiguity resolution using ionosphere-reduced virtual signals. J Geod 82:847–862

Giorgi G, Teunissen PJG, Verhagen S, Buist P (2010) Testing a new multivariate gnss carrier phase attitude determination method for remote sensing platforms. Adv Space Res 46(2):118–129

Goad C (1992) Robust techniques for determining GPS phase ambiguities. In: 6th International Geodetic Symposium on Satellite Positioning. Columbus, Ohio, pp 245–254

Hernández-Pajares M, Zomoza JMJ, Subirana JS, Colombo O (2003) Feasibility of wide-area subdecimeter navigation with GALILEO and modernized GPS. IEEE Trans Geosci Remote Sens 41(9):2128–2131

Isshiki H (2004) A long baseline kinematic GPS solution of ionosphere-free combination constrained by widelane combination. In: Oceans'04. MTTS/IEEE Techno-Ocean'04, IEEE, vol 4, pp 1807–1814.

Lawrence D (2009) A new method for partial ambiguity resolution. In: ION ITM 2009, Anaheim, CA, pp 652–663.

Li B, Teunissen PJG (2012) Real-time kinematic positioning using fused data from multiple GNSS antennas. In: 15th International Conference on Information Fusion (FUSION), Singapore, pp 933–938.

Li B, Feng Y, Shen Y (2010) Three carrier ambiguity resolution: distance-independent performance demonstrated using semi-generated triple frequency GPS signals. GPS Solut 14(2):177–184

Li B, Verhagen S, Teunissen PJG (2013) Robustness of GNSS integer ambiguity resolution in the presence of atmospheric biases. GPS Solut doi:10.1007/s10291-013-0329-5

Liu GC, Lachapelle G (2002) Ionosphere weighted GPS cycle ambiguity resolution. In: ION National Technical Meeting, San Deigo, CA, pp 1–5.

Melbourne WG (1985) The case for ranging in GPS-based geodetic systems. In: 1st International Symposium on Precise Positioning with Global Positioning System, Rockville, Maryland, vol 1, pp 373–386.

Mowlam A (2004) Baseline precision results using triple frequency partial ambiguity sets. In: ION GNSS-2004. Long Beach, CA, pp 2509–2518

Odijk D (2000) Weighting ionospheric corrections to improve fast GPS positioning over medium distances. In: ION GPS 2000. Salt Lake City, UT, pp 1113–1123

Pantoja VDG (2009) Partial ambiguity fixing for precise point positioning with multiple frequencies in the presence of biases. Thesis, Department of Electrical Engineering and Information Technology, Technical University Munich

Parkins A (2011) Increasing GNSS RTK availability with a new single-epoch batch partial ambiguity resolution algorithm. GPS Solut 15:391–402

Rao C (1973) Linear statistical inference and its applications. John Wiley and Sons, New York

Ray JK, Canon ME, Fenton P (2000) GPS code and carrier multipath mitigation using a multi-antenna system. IEEE Trans Aerosp Electron Syst 37(1):183–195

Richert T, El-Sheimy N (2007) Optimal linear combinations of triple frequency carrier phase data from future global navigation satellite systems. GPS Solut 11(1):11–19

Schaffrin B, Bock Y (1988) A unified scheme for processing GPS dual-band phase observations. Bull Géod 62(2):142–160

Takasu T, Yasuda A (2010) Kalman-filter-based integer ambiguity resolution strategy for long-baseline RTK with ionosphere and troposphere estimation. In: ION GNSS 2010. Portland, Oregon, pp 201–207

Teunissen PJG (1997) On the GPS widelane and its decorrelating property. J Geod 71:577–587

Teunissen PJG (1998a) Minimal detectable biases of GPS data. J Geod 72:236–244

Teunissen PJG (1998b) Success probability of integer GPS ambiguity rounding and bootstrapping. J Geod 72(10):606–612

Teunissen PJG (2003) Adjustment theory: an introduction. Series on mathematical geodesy and positioning. Delft University Press, Delft

Teunissen PJG (2012) A-PPP: array-aided precise point positioning with global navigation satellite systems. IEEE Trans Signal Process 60(6):2870–2881

Teunissen PJG, de Jonge P, Tiberius CCJM (1997) The least-squares ambiguity decorrelation adjustment: its performance on short GPS baselines and short observation spans. J Geod 71:589–602

Teunissen PJG, Joosten P, Tiberius CCJM (1999) Geometry-free ambiguity success rates in case of partial fixing. In: ION National Technical Meeting 1999 and 19th Biennal Guidance Test Symposium, San Diego CA, pp 201–207.

Teunissen PJG, Joosten P, Tiberius CCJM (2002) A comparison of TCAR, CIR and LAMBDA GNSS ambiguity resolution. In: ION GPS 2002, Portland, OR, pp 2799–2808.

Verhagen S, Li B (2012) LAMBDA software package: Matlab implementation, Version 3.0. Delft University of Technology and Curtin University, Perth, Australia.

Verhagen S, Li B (2013) Ps-LAMBDA software package: Matlab implementation, Version 1.0. Curtin University of Technology, Perth, Australia.

Verhagen S, Li B, Teunissen PJG (2013) Ps-LAMBDA: ambiguity success rate evaluation software for interferometric applications. Comput Geosci 54:361–376

Werner W, Winkel J (2003) TCAR and MCAR options with Galileo and GPS. In: ION GPS/GNSS 2003, Portland, OR, pp 790–800.

Wübbena G (1991) Zur Modellerung von GPS Beobachtungen fuer die hochgenaue Positionsbestimmung. University Hannover, Germany, (in German).